This is an open access article published under an ACS AuthorChoice License, which permits copying and redistribution of the article or any adaptations for non-commercial purposes.

JACS
JOURNAL OF THE AMERICAN CHEMICAL SOCIETY
Article
Cite This: J. Am. Chem. Soc. 2018, 140, 15402−15411
pubs.acs.org/JACS

# Lipid- and Cholesterol-Mediated Time-Scale-Specific Modulation of the Outer Membrane Protein X Dynamics in Lipid Bilayers

Lukas Frey,[†] Sebastian Hiller,[‡] Roland Riek,*[,†] and Stefan Bibow*[,‡]

[†]Laboratory for Physical Chemistry, ETH Zurich, 8093 Zurich, Switzerland
[‡]Biozentrum, University of Basel, 4056 Basel, Switzerland

Supporting Information

**ABSTRACT:** Membrane protein function fundamentally depends on lipid-bilayer fluidity and the composition of the biological membrane. Although dynamic interdependencies between membrane proteins and the surrounding lipids are suspected, a detailed description is still missing. To uncover lipid-modulated membrane protein backbone dynamics, time-scale-specific NMR relaxation experiments with residue-resolution were recorded. The data revealed that lipid order, modified either biochemically or biophysically, changes the dynamics of the immersed membrane protein in a specific and time-scale-dependent manner. A temperature-dependent dynamics analysis furthermore suggests a direct coupling between lipid and protein dynamics in the picosecond−nanosecond, microsecond, and millisecond time scales, caused by the lipid's *trans*−*gauche* isomerization, the segmental and rotational motion of lipids, and the fluidity of the lipid phase, respectively. These observations provide evidence of a direct modulatory capability of the membrane to regulate protein function through lipid dynamics ranging from picoseconds to milliseconds.

## INTRODUCTION

Biological membranes compartmentalize cells and harbor within their 2-dimensional matrix membrane proteins to facilitate biological functions, such as transport and signaling.[1,2] The availability of a large and complex repertoire of lipids with distinct properties furthermore suggests that lipid-bilayer composition and the active modulation of fluidity and thickness thereof is of functional relevance and evolutionarily advantageous.[3] For example, lipids with different headgroups, variable acyl chain length, and degree of unsaturation can be incorporated into a bilayer to modulate the phase state of the bilayer. In the fluid liquid-disordered ($L_D$) phase above the melting temperature $T_m$, lipids are highly dynamic, exhibiting fast rotational motions, lateral diffusion, and *trans*−*gauche* isomerization.[4,5] In the gel-like solid-ordered ($S_O$) phase below $T_m$, acyl chains are highly ordered and predominantly in *trans*-conformation. They exhibit reduced *trans*−*gauche* isomerization rates, diminished segmental and rotational motions, as well as decreased lateral mobility.[4,6,7] While an increase in the acyl chain length stabilizes the $S_O$ phase, acyl chain unsaturation favors the $L_D$ phase. Cholesterol, a sterol-type lipid, is found in biological membranes in concentrations ranging from 1 mol % up to 50 mol %.[5,8−10] Due to its rigid ring structure, cholesterol increases the order of lipid acyl chains by reducing *gauche* rotamer formation rates, thereby modifying lipid-bilayer dynamics and fluidity.[9,11,12] This physical state is referred to as the liquid-ordered ($L_O$) phase and is different from the $L_D$ and $S_O$ phases. Notably, cholesterol broadens the transition temperature zone and increases $T_m$.[5]

It is well-documented that bilayer thickness[13−16] and lipid headgroups[17] have the capability to modulate enzymatic and transport activities of membrane proteins. Remarkably, recent evidence suggests that the function of membrane proteins is governed at least in part by an interplay between lipid dynamics and membrane protein dynamics,[18,19] revealing a potential regulatory layer or even an environment-sensing mechanism as suggested by transient receptor channels involved in infrared sensing of bats and snakes.[20,21] With respect to the well-established interdependency between solvent and soluble protein dynamics,[22,23] an equivalent coupling between lipid, cholesterol, and membrane protein dynamics seems likely and may even be more pronounced and extended to a wider range of time scales, relevant for functional transport and signaling. Unfortunately, it is intrinsically difficult to determine such potential dynamic interactions with residue-resolution because of both the inability to resolve dynamic lipid and cholesterol molecules by cryo-electron microscopy and X-ray crystallography, and the lack of well-suited bilayer-based systems for solution NMR investigations. Hence, although it is important for a fundamental understanding, no

Received: August 26, 2018
Published: October 5, 2018

Downloaded via UNIV OF BASEL on September 5, 2019 at 15:25:51 (UTC).
See https://pubs.acs.org/sharingguidelines for options on how to legitimately share published articles.


© 2018 American Chemical Society

DOI: 10.1021/jacs.8b09188
J. Am. Chem. Soc. 2018, 140, 15402−15411

atomic insights into lipid-mediated modulation of membrane protein dynamics has been obtained so far. However, recent technological innovations unlocked the full potential of nanodiscs for investigations of membrane proteins with atomic details in a detergent-free lipid-bilayer environment.[18,24−27] In combination with NMR spectroscopy, lipid-bilayer nanodiscs allow for the study of membrane protein dynamics,[28,29] as well as lipid dynamics over a wide range of temperatures and lipid compositions with atomic resolution.[30−32]

To reveal a dynamic coupling between lipids and a membrane protein, we reconstituted the outer membrane protein X (OmpX) into a saturated, unsaturated, or cholesterol-containing lipid-bilayer. Using three residue-specific $^{15}$N-based NMR relaxation experiments for the membrane protein,[33,34] each of which is especially sensitive in the $10^{10}-10^{9}$, $10^{5}$, and $10^{4}-10^{3}$ s$^{-1}$ motional regime, as well as $^{13}$C-based $R_1$ and $R_2$-CPMG relaxation experiments for the lipids, we observed that membrane protein backbone dynamics are intimately connected to specific lipid dynamics on specific time scales. The fact that such lipid-induced membrane protein dynamics can be observed for the rather rigid $\beta$-barrel OmpX points toward the widespread presence of lipid-orchestrated dynamics of membrane proteins.

## RESULTS

**Membrane Bilayer Composition Influences Membrane Protein Dynamics.** To investigate lipid-dependent membrane protein dynamics, we reconstituted $^{2}$H,$^{13}$C,$^{15}$N-labeled OmpX into nanodiscs composed of either saturated, unsaturated, or cholesterol-containing unsaturated lipid bilayers. The lipids of choice were thereby *cis*-9-tetradecanoyl-*sn*-3-glycero-3-phosphocholine (*cis*-9-unsaturated 1,2-dimyristoyl-*sn*-glycero-3-phosphocholine, here termed DMPC14:1) and its saturated counterpart (DMPC14:0). The consequences from unsaturation are a lower melting temperature $T_m$ of 270 K in nanodiscs (269 K in liposomes[35]) compared to its saturated counterpart with a $T_m$ of 298 K in nanodiscs (298 K in liposomes,[5] Figure 1). The agreement with previously determined $T_m$ for DMPC14:0 and DMPC14:1 indicates that nanodiscs represent a suitable system to study lipid-bilayer-related dynamic effects.

In a first step, the dynamics of OmpX were probed at 316 K in DMPC14:1 (Figure 2a−c), DMPC14:1 with ca. 15% cholesterol (Figure 2d−f), and DMPC14:0 (Figure 2g−i) by the collection of $^{15}$N-based $R_1$, $R2_{R1\rho}$, and $R_2$ NMR relaxation data which are mainly sensitive to picosecond−nanosecond (ps−ns), microsecond ($\mu$s), and millisecond (ms) time scale motions, respectively.

The analysis of relaxation data at 316 K for OmpX in saturated DMPC14:0 (Figure 2g−i) showed profiles that were identical to those determined previously.[29] Loop residues exhibit higher $R_1$ and $R_2$ and lower $R2_{R1\rho}$ values compared to $\beta$-strand residues, revealing significant nanosecond time scale motions as well as conformational exchange on the high microsecond to millisecond time scale, that are largely different and independent from motions of the rigid $\beta$-barrel (Figure 2g−i). The striking presence of "dynamic ramps", connecting the fast movements of dynamic loops with the slower $\beta$-barrel dynamics, is especially pronounced at the edges of $\beta$-strands $\beta$3, $\beta$4, $\beta$5, and $\beta$6 (dotted lines in Figure 2h). Interestingly, these ramp-like transitions between the $\beta$-strands and the loops are attenuated for OmpX in unsaturated DMPC14:1 (Figure 2b). In fact, a step-like behavior in the $R2_{R1\rho}$ relaxation data for

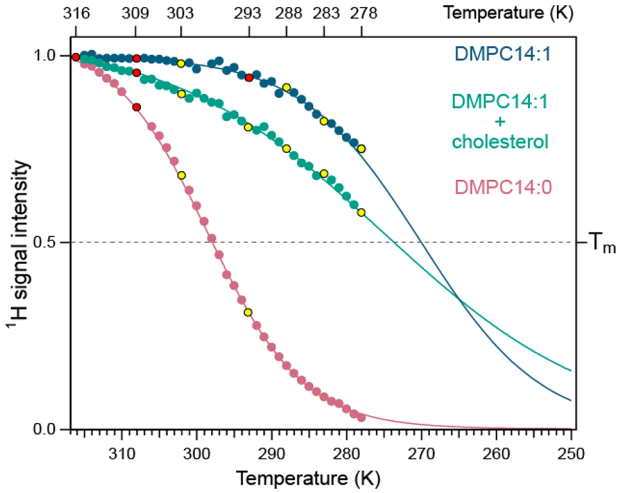


**Figure 1.** Temperature-dependent signal intensity changes of lipids in nanodiscs report on the lipid phase transition temperature. The intensities of acyl chain proton signals are plotted against the temperature, normalized to the intensity at 316 K. The NMR signals for protons attached to the C4−C11 acyl chain carbons are used. The phase transition temperature $T_m$, indicated with a horizontal line, represents the temperature at which the transition from liquid to gel ($S_O$ phase) is one-half complete. For DMPC14:0 (red) a $T_m$ of 298 K (literature value 298 K), for DMPC14:1 (blue) a $T_m$ of 270 K (literature value 269 K), and for DMPC14:1 with ca. 15% cholesterol (green) a $T_m$ of 274 K were found in nanodiscs. The intensities were fitted using a sigmoidal curve. The addition of cholesterol to DMPC14:1 changes the liquid phase from a liquid-disordered ($L_D$) to a liquid-ordered ($L_O$) phase and broadens the transition compared to pure DMPC14:1, in agreement with previous reports. Relaxation data for OmpX immersed in the above-mentioned lipid environments were extracted and analyzed at temperatures indicated by red dots (Figure 2 and 4), whereas a qualitative assessment of OmpX microsecond-millisecond motions was conducted at temperatures indicated by yellow dots (Figure 5).

the loops and edges of the $\beta$-strands $\beta$4 and $\beta$6 is present and indicates an uncoupling of loop and strand dynamics, similar to what has been observed for OmpX and OmpA embedded in detergent micelles.[29,36] Taken together, the comparison reveals that OmpX in the unsaturated DMPC14:1 lipid bilayer exhibits a less pronounced variability of $\beta$-strand dynamics compared to OmpX in the saturated DMPC14:0 lipid bilayer, which is more clearly visualized by a correlation plot of the spectral densities at $J(0)$ and $J(\omega_N)$ for the $\beta$-strand residues (Supporting Information Figure S1).

Strikingly, the conversion from the liquid-disordered $L_D$ to the liquid-ordered $L_O$ phase by addition of cholesterol (Supporting Information Figure S2) to the unsaturated DMPC14:1 bilayer reintroduces the dynamic ramps for the edges of $\beta$-strands $\beta$4 and $\beta$6 of OmpX (Figure 2e and Supporting Information Figure S1). The induced dynamic alterations are due to the DMPC14:1/cholesterol bilayer that exhibits a broadened gel-to-liquid phase transition. Above the $T_m$, cholesterol decelerates acyl chain segmental motions and reduces fluidity (Figure 1) which appears to be the reason for the reintroduced dynamic ramps. Those motions typically take place in the time scale of up to low microseconds.[37,38] Notably, the absence of cholesterol-dependent chemical shifts (Supporting Information Figure S3) suggests that the phase state of the lipid-bilayer modulates OmpX dynamics and not a specific cholesterol interaction.


DOI: 10.1021/jacs.8b09188
J. Am. Chem. Soc. 2018, 140, 15402−15411

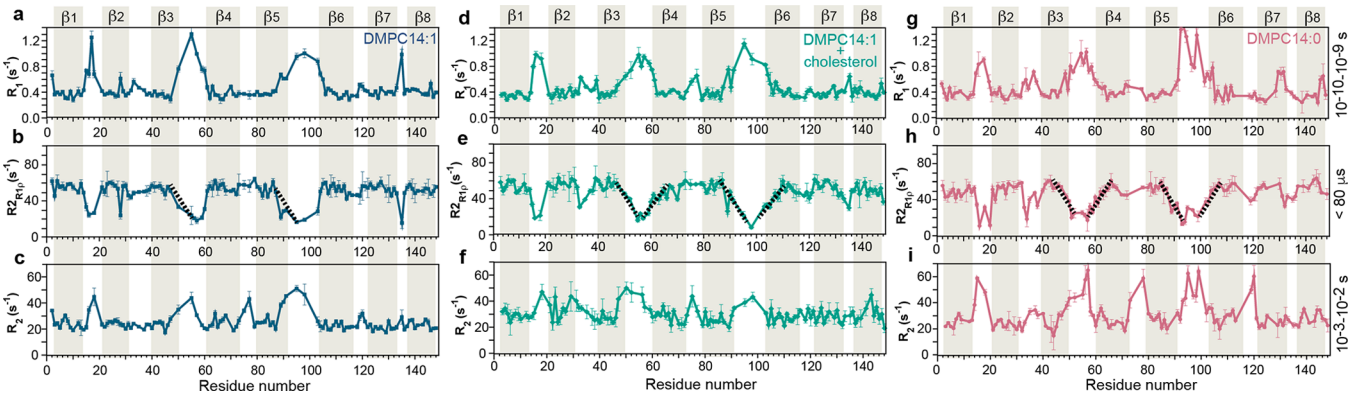


**Figure 2.** Backbone dynamics of OmpX at the picosecond–nanosecond, microsecond, and millisecond time scale. Relaxation rate constants for OmpX were measured at 316 K in three different lipid environments. (a–c) OmpX in DMPC14:1. (d–f) OmpX in DMPC14:1 with ca. 15% cholesterol. (g–i) OmpX in DMPC14:0. $R_1$ relaxation rates are sensitive to picosecond–nanosecond motions; $R2_{R1\rho}$ relaxation rates are sensitive to microsecond motions, and $R_2$ relaxation rates are sensitive to millisecond motions. The sensitive motional regimes are also indicated on the right. Dynamic ramps are emphasized with black dotted lines.

**Lipid Phase Behavior in Nanodiscs.** The hypothesis that the phase properties of the lipid bilayer influence the membrane protein dynamics hints to membrane fluidity (or lipid order) as a key modulator which we decided to investigate more thoroughly. Because the degree of fluidity of a lipid bilayer can be manipulated by temperature, we rationalized that temperature-dependent NMR measurements on lipids may give further insights into membrane dynamics. Although a large number of studies investigated lipid dynamics in liposomes using various methods,[12,38−40] only little data of lipid dynamics in nanodiscs is available.[32,41] To utilize the $^{13}$C natural abundance of lipids, we reconstituted $^{2}$H,$^{15}$N-labeled OmpX into nanodiscs containing either DMPC14:1, DMPC14:1 with cholesterol, or DMPC14:0. By using the $^{13}$C inversion recovery experiments, $R_1$ relaxation rates of lipid carbons were determined (Figure 3a–c). An increase of $R_1$ rates for C$\gamma$-, C4–C11-, and C14-carbons upon temperature decrease was observed within all three lipid bilayers. Because a temperature decrease is accompanied by an increase of the rotational tumbling time $\tau_c$ of the nanodisc, which encloses the lipid bilayer (Supporting Information Figure S4), an increase in the lipids $R_1$ relaxation rates means that the carbons of the lipids exhibit dynamics that are in the fast motion limit. The fast motion limit is separated from the slow motion limit by an $R_1$ maximum ($T_1$ minimum), which corresponds to 1.06 ns on a 600 MHz spectrometer for $^{13}$C. Hence, increasing $R_1$ rates upon temperature reduction indicate motions that are faster than 1.06 ns, as would be expected for a small and flexible molecule. Notably, lipid $^{13}$C $R_1$ rates for C4–C11 vary with the field strength. This field dependence reveals that the measured C8 and C11 lipid relaxation rates are close to the $R_1$ maximum, therefore reporting on picosecond motions in the hundreds of picoseconds range (Supporting Information Figure S5). Importantly, $R_1$ values for the C8- and C11-carbons increase upon addition of cholesterol, directly evidencing a deceleration of acyl chain motions. That substantiates the notion that $R_1$ rates report on *trans–gauche* isomerization motions that are found on the time scale of hundreds of picoseconds. As can be seen, $R_1$ rates are furthermore sensitive to the proposed *trans–gauche* isomerization rate reduction upon cholesterol addition.[12] The C14-carbons of all three lipid compositions exhibit similar but significantly reduced $R_1$ rates compared to carbons that are located more centrally within the acyl chain. In the fast motion limit, smaller $R_1$ values for C14 report on picosecond motions that are faster than the picosecond motions found for the C8 and C11 carbons (Figure 3b). Interestingly, the headgroup C$\gamma$-carbons show identical $R_1$ rates for all three lipid environments at temperatures between 316 K and around 298 K, the melting temperature $T_m$ of DMPC14:0 (Figure 3c). A further reduction of temperature induces a more rapid increase of $R_1$ rates for C$\gamma$ from DMPC14:0 compared to DMPC14:1. Notably, at this temperature $R_1$ relaxation rates begin to decline for the C2-carbon of DMPC14:0 (Supporting Information Figure S5), located in immediate vicinity to the most rigid region of the lipid, the glycerol backbone. The $R_1$ maximum (equivalent to the $T_1$ minimum) of the C2-carbon reveals a $\tau_c$ of around 1 ns at 300 K (Supporting Information Figure S5). These observations indicate the beginning impact of restricted rotational or wobbling motion on $R_1$ due to reduced fluidity of the DMPC14:0 bilayer near the $T_m$.

To gain further insights into lipid fluidity, we recorded $^{13}$C CPMG experiments to extract $R_2$ relaxation rates. Initial experiments used a CPMG-frequency $\nu_{cpmg}$ = 250 Hz, refocusing dynamic contributions to $R_2$ that are slower than $(2\pi^*\nu_{cpmg})^{-1}$ = 636 $\mu$s. Integration of the signals for carbon atoms C4–C11 reveals a behavior of the transverse relaxation rates that correlates with the previously observed $^{1}$H lipid intensities (Figure 1 and Figure 3d). Similar $R_2$ rates for C4–C11 are observed at 316 K within the three lipid environments. However, upon reduction of temperature the relaxation rates for DMPC14:0 increase dramatically. In contrast, only moderate increases in relaxation rates for DMPC14:1 and DMPC14:1 with cholesterol are observed. The reason for the strong increase of $R_2$ for DMPC14:0 is likely due to a strong impact of slower microsecond motions on carbon dynamics, triggered by reduced bilayer fluidity. To validate our assumption, we repeated the CPMG experiment with a CPMG-frequency of 2000 Hz (refocusing motions slower than 80 $\mu$s). Indeed, $R_2$ rates for DMPC14:0 are significantly reduced near and below $T_m$ (Figure 3e) but are still much higher than that for DMPC14:1, whose $R_2$ rate does not appear to be affected by motions slower than 80 $\mu$s. Notably, the difference between the two $R_2$ rates ($\nu_{cpmg}$ = 250 Hz and 2 kHz) is negligible for DMPC14:0 at 316 K but increases with decreasing temperature above the $T_m$.


DOI: 10.1021/jacs.8b09188
J. Am. Chem. Soc. 2018, 140, 15402−15411

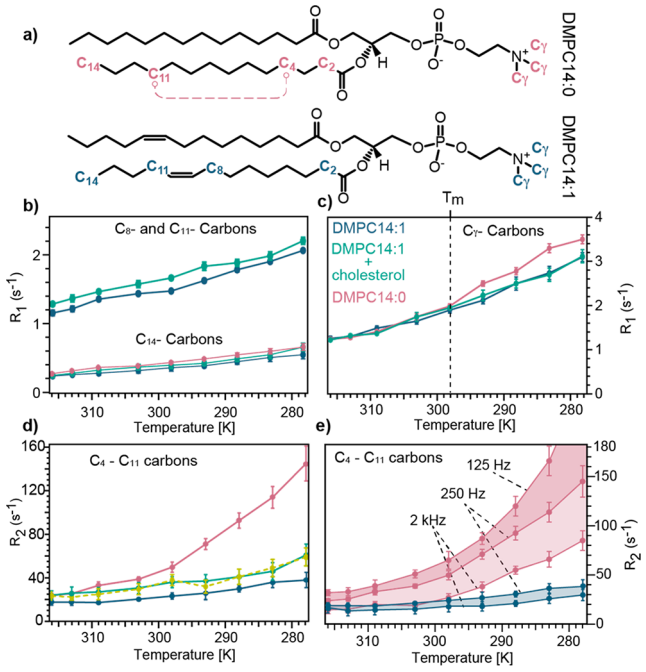


**Figure 3.** Temperature-dependent relaxation rates of lipids in OmpX-containing nanodiscs. $^{13}C$ relaxation rate constants for lipids are plotted against the temperature. The temperature was reduced from 316 K, where DMPC14:0 and DMPC14:1 are found in the liquid-disordered phase and DMPC14:1 with cholesterol is found to be in the liquid-ordered phase. At 278 K, DMPC14:0 transitioned into the solid-ordered phase. (a) Representation of DMPC either with its saturated acyl chain (termed DMPC14:0) or 9-*cis* unsaturated acyl chain (termed DMPC14:1). Carbon atoms for which relaxation rates were extracted are indicated. (b) $R_1$ relaxation rates of C14 as well as C8 and C11 are plotted against the temperature. Addition of cholesterol to DMPC14:1 increases $R_1$ rates of C8 and C11. (c) Relaxation rates for the C$\gamma$ carbons are plotted against the temperature, showing identical $R_1$ rates for all three lipid environments until 298 K, the melting temperature of DMPC14:0 (indicated with a dashed line). (d) $R_2$ relaxation rates for the C4−C11 carbons are plotted against the temperature that were measured with a CPMG-frequency of 250 Hz. The yellow dotted line shows relaxation rates for another assembly with DMPC14:1 and cholesterol to confirm relaxation rates and test reproducibility. (e) $R_2$ relaxation rates for the C4−C11 carbons of the acyl chain measured with additional CPMG-frequencies of 125 and 2000 Hz. The $R_2$ rate for DMPC14:0 at 278 K with a CPMG-frequency of 125 Hz was 242 ± 20 $s^{-1}$, but was excluded in the graph for visibility reasons. CPMG $R_2$ rates for DMPC14:1 with cholesterol can be found in Supporting Information Figure 5. Please note the similar color code but different axis ranges for parts b−e.

By changing the CPMG-frequency to 125 Hz, motions up to 1.2 ms contribute to $R_2$. As can be seen, only below the $T_m$ of DMPC14:0 do $R_2$ rates become strongly influenced by motions slower than 636 $\mu$s. Taken together, low microsecond motions contribute to $^{13}C$ $R_2$ well above the $T_m$. Upon temperature reduction, reduced lipid fluidity due to restricted rotational and segmental lipid motions goes along with an increasing amount of microsecond motions that become slower near and at its $T_m$, eventually reaching the millisecond time scale below the $T_m$.

**Membrane Protein Picosecond and Nanosecond Motions Report on Lipid *Trans*−*Gauche* Isomerization.** To investigate the impact of lipid dynamics on the membrane protein further, we conducted temperature-dependent $^{15}N$ relaxation measurements on the outer membrane protein X. A temperature change within the liquid-disordered $L_D$ and the liquid-ordered $L_O$ phase was conducted, experimentally realized by using DMPC14:1 without and with cholesterol, respectively. Furthermore, a temperature change within the $L_D/S_O$ phase transition zone was conducted, experimentally realized by using DMPC14:0 (Figure 1).

For DMPC14:1, a temperature reduction from 316 to 309 K lies within the $L_D$ phase and therefore does not change the phase state of the lipids significantly (Figure 1). As an initial step, $R_1$ relaxation rates at different temperatures were recorded (Supporting Information Figure S6). Notably, $^{15}N$ $R_1$ depends on the molecular tumbling time $\tau_c$ that changes with temperature. To extract motional differences at 316 and 309 K that are not due to $\tau_c$-differences, the $^{15}N$ relaxation rates were corrected according to the measured tumbling times $\tau_c$ using $\beta$-barrel residues (see Experimental Section). Similar to $^{13}C$ $R_1$ rates, rate changes for $^{15}N$ $R_1$ upon temperature reduction depend on the motional regimes (fast or slow), that are separated by the $R_1$ maximum. On a 600 MHz spectrometer, the $R_1$ maximum is $(\omega_N)^{-1}$ = 2.65 ns for $^{15}N$. $R_1$ of $^{15}N$ will increase upon temperature reduction if the decelerated motions remain faster than 2.65 ns (motions fall within the fast motional regime but move toward the $R_1$ maximum). On the other hand, $^{15}N$ $R_1$ decreases upon temperature reduction when nanosecond motions slower than 2.65 ns decelerate (motions fall within the slow motional regime). A prime example for this temperature-dependent behavior is the domain of the Sendai virus nucleoprotein, whose termini exhibit an opposite $R_1$-behavior upon temperature reduction compared to that of the central part of the protein.[42] Increased $R_1$ values for OmpX residues in flexible loops therefore indicate correlation times that are closer to the $R_1$ maximum than the correlation times for rigid $\beta$-barrel residues, as it would be expected (Supplementary Figure 6). Note that we determined the $\tau_c$-values from residues exhibiting $\beta$-strand chemical shifts. The $\tau_c$-correction thus utilized $\beta$-barrel residues but not loop residues which are therefore not $\tau_c$-corrected.

As it can be seen, $\Delta R_1^*$ values for $\beta$-barrel residues are positive (Figure 4a). This increase of $\tau_c$-corrected $^{15}N$ $R_1$ rates for rigid $\beta$-barrel residues is unexpected, because an increase of $^{15}N$ $R_1$ rates indicates a deceleration of motions that are faster than 2.65 ns. Since the majority of $\beta$-barrel residues are rigid, N−H bond vector motions from the fast motional regime must be due to fast lipid motions since they are nearby OmpX backbone N−H vectors and faster than 2.65 ns.

By performing the same temperature change with DMPC14:1 and 15% cholesterol, i.e., within the $L_O$ phase, $\Delta R_1^*$ rates for DMPC14:1 $\beta$-strands (e.g., $\beta$1, $\beta$2, $\beta$4, $\beta$6) exhibit negative $\Delta R_1^*$ values, indicating this time a deceleration of motions that are slower than 2.65 ns. As we observed before, the reorganization of the bilayer from the $L_D$ to a $L_O$ phase upon cholesterol addition increases lipid $R_1$ rates (Figure 3), due to reduced *trans*−*gauche* formation rates.[12,43] Furthermore, also $^{15}N$ $R_2$ rates for DMPC14:1 with cholesterol are increased when compared to DMPC14:1 without cholesterol. The combined relaxation rate changes upon cholesterol addition may therefore be responsible for the time scale shift of lipid motions, resulting in apparent $R_1$ changes for OmpX motions that now fall within the slow motional limit for annular lipids.[44] The protein therefore displays negative $\Delta R_1^*$ values for rigid $\beta$-strand residues in DMPC14:1 with


DOI: 10.1021/jacs.8b09188
J. Am. Chem. Soc. 2018, 140, 15402−15411

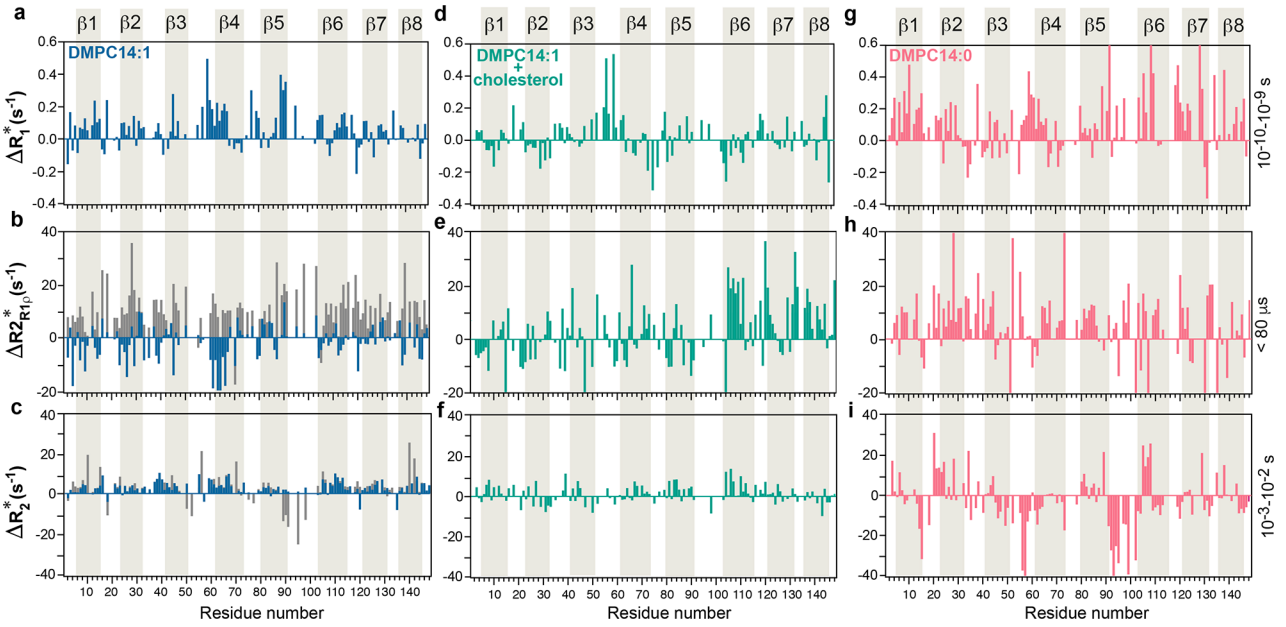


**Figure 4.** Difference plot of the OmpX backbone dynamics at the nanosecond, microsecond, and millisecond time scale. The difference in relaxation rates between different temperatures is shown for all three lipid environments. (a–c) Relaxation rate differences for OmpX in DMPC14:1 between 309 and 316 K (309–316 K) are shown as blue bars. In parts b and c, gray bars indicate the difference in relaxation rates between 293 and 316 K. (d–f) Relaxation rate differences for OmpX in DMPC14:1 with cholesterol between 309 and 316 K (309–316 K) are shown as green bars. (g–i) Relaxation rate differences for OmpX in DMPC14:0 between 309 and 316 K (309–316 K) are shown as red bars. Since the molecular tumbling influences the relaxation rates and changes with temperature, the relaxation rates at 309 and 293 K were scaled by experimentally determined tumbling times $\tau_c$ (see Experimental Section).

cholesterol (Figure 3d). Although $^{15}$N $R_1$ is most sensitive to motions close to $(\omega_N)^{-1}$ = 2.65 ns, we would like to emphasize that $^{15}$N $R_1$ is also sensitive to motions that are close to $(\omega_H + \omega_N)^{-1}$ = 241 ps and $(\omega_H - \omega_N)^{-1}$ = 295 ps, on approximately the time scale of *trans–gauche* isomerization. In a hypothetical case of a relatively invariable amount of motions at $(\omega_N)^{-1}$ = 2.65 ns between 316 and 309 K, an increasing (decreasing) amount of motions at $(\omega_H \pm \omega_N)^{-1}$ upon temperature decrease would also result in positive (negative) $\Delta R_1^*$ rates for rigid $\beta$-strand residues, revealing changes in *trans–gauche* isomerization rates via $^{15}$N $R_1$'s sensitivity to hundreds of picoseconds. Notably, for OmpX in DMPC14:0, $\Delta R_1^*$ values for $\beta$-strands in the $L_D/S_O$ phase transition zone are again predominantly positive (Figure 3g), indicating that motions faster than 2.65 ns are again imposed on the rigid $\beta$-strand residues. In summary, $^{15}$N relaxation measurements revealed a dynamic coupling in the ps–ns time scale between the lipid environment and the immersed membrane protein OmpX. $\beta$-Barrel $^{15}$N $R_1$ values changes are specific to the lipid phases which exhibit different lipid *trans–gauche* isomerization rates (Figure 3).

**Lipid Segmental and Rotational Motions Influence Protein Dynamics in the Microsecond Time Scale.** $^{15}$N $R2_{R1\rho}$ experiments were conducted with a 2000 Hz radio frequency field, refocusing dynamic contributions to $^{15}$N $R_2$ that are slower than 80 $\mu$s. $R2_{R1\rho}$ rate constants increase at 309 K for DMPC14:1, DMPC14:1 with cholesterol, and DMPC14:0 (Supporting Information Figure S6). This indicates a uniform change of protein dynamics on motions faster than 80 $\mu$s, either due to bilayer-related changes, such as altered segmental and rotational motions, occurring on low microsecond[37] and hundreds of nanoseconds,[38] respectively, or due to temperature-related $\tau_c$-changes. Indeed, correcting the $R2_{R1\rho}$ rate constants found at 309 K for differences in $\tau_c$ changes the picture and reveals positive and negative $\Delta R2^*_{R1\rho}$ values for DMPC14:1, however, with predominantly negative $\Delta R2^*_{R1\rho}$ values for DMPC14:1 $\beta$-barrel residues (Figure 4b, blue bars). This indicates slightly diminished OmpX dynamics for motions faster than 80 $\mu$s. Interestingly, this agrees with slightly diminished $R_2$ values for DMPC14:1 at 309 K (Figure 3e). For OmpX in DMPC14:1 with cholesterol, no clear trend can be observed (Figure 4e).

In contrast, OmpX in DMPC14:0 has larger $R2_{R1\rho}$ values at 309 K even after $\tau_c$-correction, resulting in positive $\Delta R2^*_{R1\rho}$ values (Figure 4h). These differences in $R2_{R1\rho}$ relaxation rates can neither be solvent-viscosity-related nor $\tau_c$-related since the temperature shift was equal for all samples and all relaxation values were $\tau_c$-corrected. Nor can it be explained with variations in the rotational motion of OmpX since the rotational correlation time $\tau_c$ and therefore the activation energies of the rotational motion are similar for OmpX in DMPC14:0, DMPC14:1, and DMPC14:1 with cholesterol with values of 14.7, 17.4, and 15.1 kcal/mol, respectively (Supporting Information Figure S4). Consequently, enhanced membrane protein microsecond motions in DMPC14:0 must have a lipid-dependent origin. Indeed, our lipid measurements with a CPMG-frequency of 2000 Hz revealed that $^{13}$C $R_2$ rates increase by ca. 23% from 14.7 $s^{-1}$ (at 316 K) to 19 $s^{-1}$ (at 309 K) for DMPC14:0 (Figure 3). Increased lipid microsecond motions are linked to decelerated lipid segmental and lipid rotational motions upon temperature reduction, that influence membrane protein microsecond motions. To support this argumentation, we recorded $^{15}$N $R2_{R1\rho}$ relaxation rates for DMPC14:1 at 293 K, a temperature that shows a similar increase of lipid $^{13}$C $R_2$ values than DMPC14:1 (from 13.8 to 17 $s^{-1}$) and can therefore be considered the very beginning of the $L_D$ to $S_O$ phase transition for DMPC14:1 (Figures 1 and 3 and Supporting Information Figure S6). Strikingly, mostly


DOI: 10.1021/jacs.8b09188
J. Am. Chem. Soc. 2018, 140, 15402–15411

positive $\Delta R2^{*}_{R1\rho}$ values are now observed (Figure 3b, gray bars), similar to the results for OmpX in DMPC14:0. We therefore attribute positive $\Delta R2^{*}_{R1\rho}$ values to decelerated segmental and rotational lipid motions, that increase the amount of microsecond motions for the immersed membrane protein above the $T_m$ (Figure 3).[12,37,38]

**Membrane Protein Millisecond Motions Depend on Bilayer Fluidity.** Significant changes in millisecond motions for OmpX upon temperature decrease are only found in DMPC14:0 (Supporting Information Figure S6), in agreement with significantly reduced $^1$H lipid signal intensities (Figure 1), and increased $^{13}$C lipid $R_2$ rates (Figure 3e). As expected, $\Delta R_2^{*}$ values remain small for OmpX in DMPC14:1 even when taking the difference between 316 and 293 K (gray bars in Figure 4c), since the $T_m$ is at around 270 K, 28 K lower than for DMPC14:0 (Figure 1), and no significant amount of lipid motions slower than 80 $\mu$s are observed in this temperature range (Figure 3).

High microsecond to millisecond motions ($10^4$–$10^3$ s$^{-1}$) are generally difficult to quantify with solution-state NMR since they usually fall within the intermediate motional regime, leading to the disappearance of NMR signals. The early onset and deteriorating impact of these motions are exemplified by comparing the spectral quality of OmpX in DMPC14:0 and DMPC14:1 already at 303 K (Supporting Information Figure S7). In order to get qualitative insights into millisecond motions, we used the temperature-dependent spectral quality of 2D [$^{15}$N,$^1$H]-TROSY spectra as a qualitative measure for these dynamics. For OmpX in DMPC14:0, a strong line-broadening of $\beta$-barrel resonances was observed upon reduction of the temperature toward the $T_m$, resulting in reduced signal intensities which almost completely disappear at 293 K (Figure 5c and Supporting Information Figure S7). This observation cannot solely be attributed to the increase of the tumbling time, since unbroadened spectra can be recorded for OmpX in DMPC14:1 with cholesterol, exhibiting similar tumbling times (Supporting Information Figure S4). Furthermore, the loss of $\beta$-barrel resonances is not caused by sample degradation or irreversible unfolding, since increasing the temperature to 316 K retained the same high-quality spectrum of OmpX (Figure 5c). For OmpX reconstituted in DMPC14:1, the line broadening effects take effect in a temperature-shifted manner at 278 K, i.e., with a shift of 15 K relative to DMPC14:0 (Figure 4a and Supporting Information Figure S6). Thereby, the presence or absence of 15% cholesterol has no impact on the line broadening in DMPC14:1 at higher temperatures while a stronger signal intensity decrease for $\beta$-barrel resonances is found for DMPC14:1 with cholesterol upon temperature reduction (Supporting Information Figure S7), in agreement with the stronger signal intensity decay of lipids (Figure 1).

A look at the lipid $^{13}$C $R_2$ for DMPC14:0 reveals that motions slower than 80 $\mu$s increase dramatically upon approaching the $T_m$. At 303 K a significant impact on $R_2$ is due to motions between 80 and 636 $\mu$s (Figure 3e). The amount of slower microsecond motions increases further at lower temperatures and increases $R_2$ by about 50% at the $T_m$ of DMPC14:0. A different picture is revealed for DMPC14:1. Even at 278 K an insignificant amount of motions between 80 and 636 $\mu$s can be observed (Figure 3e). Hence, the loss of OmpX signals in DMPC14:0 at high temperature must be attributed to an increase of slow microsecond lipid dynamics that induce intermediate time scale field fluctuations next to the immersed membrane protein. While the origin of these motions is clearly correlated to $T_m$ and microsecond lipid motions, the exact molecular nature is unknown. The dramatic increase of lipid $R_2$ near and below the $T_m$ may be explained by the formation of metastable gel clusters.[45] The loss of OmpX signals in DMPC14:1 at low temperature (278 K) but above $T_m$ can be attributed to a strong increase of $\tau_c$ since lipid $R_2$ rates remain low even at 278 K.

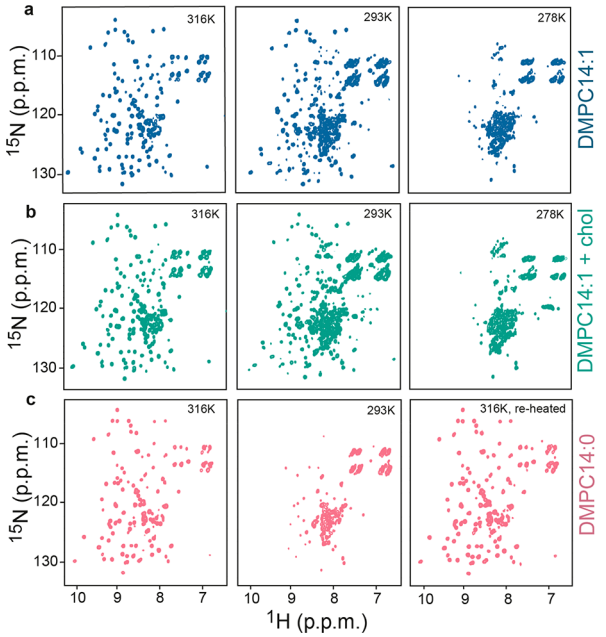


**Figure 5.** Spectral quality changes of OmpX in nanodiscs: (a) 2D [$^1$H, $^{15}$N]-TROSY spectra of OmpX in DMPC14:1 at the indicated temperatures, (b) 2D [$^1$H, $^{15}$N]-TROSY spectra of OMPX in DMPC14:1 with cholesterol at the indicated temperatures, and (c) 2D [$^1$H, $^{15}$N]-TROSY spectra of OmpX in DMPC14:0 at the indicated temperatures. A $T_m$-dependent disappearance of OmpX resonances in DMPC14:0 is evident.

Taken together, the temperature-dependent disappearance of OmpX $\beta$-barrel resonances in DMPC14:0 above 300 K are due to increased $\mu$s–ms dynamics that correlate with an increasing amount of slow microsecond lipid motions (increased $^{13}$C $R_2$ rates of DMPC14:0). These motions are due to restricted and decelerated lipid segmental and rotational motions. Reduced bilayer fluidity therefore increases not only the amount of $\mu$s–ms motions of lipids but also of the immersed membrane protein.

## CONCLUSION

The NMR data presented here have demonstrated at the single residue level that changes in lipid dynamics, introduced either by lowered temperature or by the presence of an order-inducing sterol, are transmitted in a time-scale-specific manner to an immersed membrane protein, the outer membrane protein X. Lipids within the liquid-disordered $L_D$ phase (well above the $T_m$) exhibit motions that include *trans–gauche* transitions with a frequency of around $10^{10}$ s$^{-1}$, segmental motions with a frequency of around $10^6$–$10^8$ s$^{-1}$, and rotational motions with a frequency of around $10^7$–$10^8$ s$^{-1}$.[5,37] When immersed in such a liquid bilayer environment the membrane protein backbone dynamics can only be influenced at these time scales (i.e., $10^6$–$10^{10}$ s$^{-1}$). Addition of cholesterol alters the lipid phase from a liquid-disordered


DOI: 10.1021/jacs.8b09188
J. Am. Chem. Soc. 2018, 140, 15402–15411

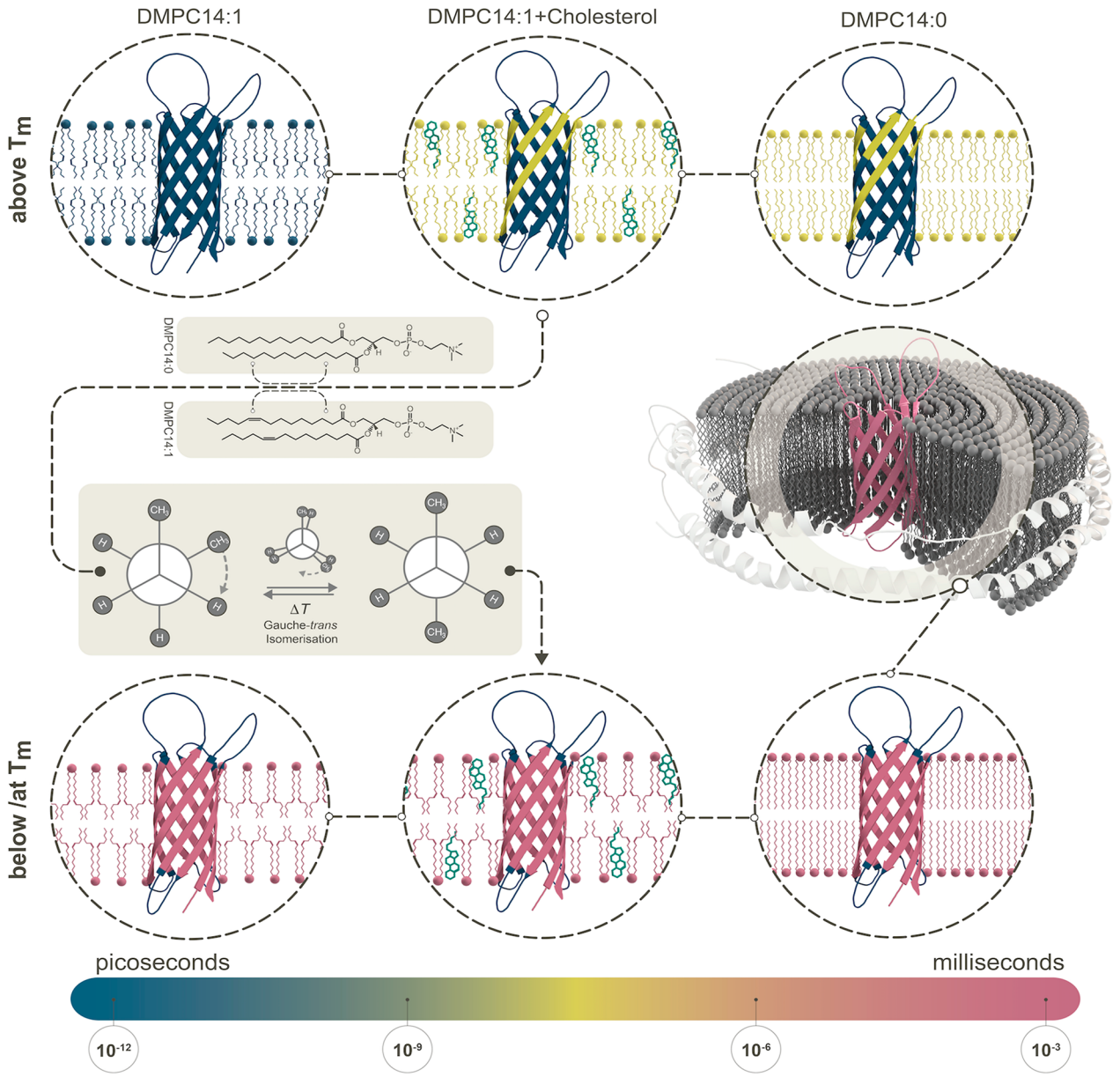


**Figure 6.** Summary of the lipid-mediated and time-scale-specific modulation of membrane protein dynamics. Lipids mediate their dynamics in the ps−ns (blue), $\mu$s (yellow), and ms (red) time scale to the nearby membrane protein. Here, the data of OmpX are shown. These motions originate from *trans*−*gauche* isomerization (ps−ns) and change with temperature, saturation (DMPC 14:0), unsaturation (DMPC 14:1), or the addition of cholesterol (green) as indicated by the color code. Upon cooling, all intrinsic lipid motions shift to the microsecond/millisecond time scales (indicated by red lipids) inducing a phase change accompanied by microsecond/millisecond dynamics on the protein.

phase ($L_D$) to a liquid-ordered phase ($L_O$ phase), which shifts the *trans*−*gauche* isomerization motion to a slower rate (Figure 3).[12] $R_1$ rates of OmpX are affected differently in the $L_O$ and $L_D$ phase, which we attribute to the order-inducing cholesterol and reduced *trans*−*gauche* isomerization rates. Furthermore, the broadening of the phase transition due to cholesterol addition reduces bilayer fluidity above $T_m$ by restricted rotational and segmental movements of lipids, leading to increased microsecond motions (Figure 3).[46] Finally, lipids in the $L_D$−$S_O$ phase transition zone feature decelerated lipid dynamics, and the phase transition from $L_D$ to $S_O$ manifests in increased microsecond and millisecond time scale dynamics, modulating the protein at even longer time scales (Figures 3 and 5). The lipid CPMG data show that, upon entering the phase transition from high temperature, microsecond motions change first, before millisecond motions are affected by reduced lipid fluidity due to restricted rotational, diffusional, and segmental motions of lipids.

It is well-known that dynamics in the microsecond or millisecond time scale are crucial for protein function.[47] Altered membrane dynamics from the nanosecond to the millisecond time scale caused by lipids, cholesterol, or temperature can therefore have a direct impact on the regulation of the biological activity membrane proteins. This dynamic interplay can be further changed by adding suitable chemical molecules, providing a powerful tool to modulate and regulate the function of membrane proteins through a dynamic control. It is thus not surprising that nature changes the composition of biological membranes in a physiology-dependent manner by the use of a plethora of lipids that could


DOI: 10.1021/jacs.8b09188
J. Am. Chem. Soc. 2018, 140, 15402−15411

modulate protein dynamics and thus function. Microdomains and leaflet asymmetry may therefore even allow for a spatially restricted and directional protein response. Strikingly, the membrane environment provides a repertoire to regulate functions of immersed proteins via dynamics that lie between picoseconds and milliseconds, which is substantially larger compared to its aqueous counterpart, that can influence the protein dynamics only at the picosecond and nanosecond time scales (Figure 6).

## EXPERIMENTAL SECTION

**Expression in Perdeuterated M9 Medium and Refolding of OmpX.** *E. coli* outer membrane protein X (OmpX) was expressed in *E. coli* strain BL21 (DE3) Star (Invitrogen, Carlsbad) using M9 minimal medium ($^2$H, $^{13}$C, $^{15}$N). In a first step a single colony of the transfected OmpX cells was inoculated for 8 h (or $OD_{600}$: 0.4−0.5) at 37 °C and 220 rpm in a 10 mL portion of $^2$H LB-medium. The preculture was subsequently added to 500 g of M9 medium using 2.5 g/L D-glucose $^{13}C_6$ 1,2,3,4,5,6,6-$d_7$ (SigmaAldrich) and was grown overnight at 37 °C, 120 rpm. After addition of 600 g of M9 medium the culture was grown to an $OD_{600}$ 0.4−0.6, and then overexpression of OmpX was induced by adding 1 mM isopropyl $\beta$-D-1-thiogalactopyranoside (IPTG; Invitrogen, Carlsbad). After 15 h of overexpression, the cells were harvested by centrifuging at 5000*g*, 4 °C for 10 min, and were resuspended in 100 mL of lysis buffer (20 mM Tris, 5 mM EDTA, pH 8). After gentle stirring for 30 min at 4 °C, the cells were lysed by passing twice through the microfluidizer at a pressure of 42 psi. OmpX was purified as described earlier[48] and then refolded in a dropwise manner by addition of 5 mL of OmpX solution to 50 mL of 50 mM Tris, 100 mM NaCl, 0.5% dodecylphosphocholine (FC-12; Avanti Polar lipids), 500 mM L-arginine, pH 8.5. After gentle stirring for 2 h at room temperature, OmpX was dialyzed three times against 4 L buffer (20 mM Tris, 100 mM NaCl, pH 7.4) using a 6−8 kDa membrane. OmpX was concentrated using an Amicon Ultra-4 10.000 Da molecular weight cutoff (MWCO) concentrator (Merck) to a concentration of ∼600 $\mu$M and stored after freezing at −80 °C.

**Expression of MSPΔH5.** The plasmid (pET-28a) with the coding sequence of truncated apoA-I missing residues 1−54 and 121−142 (MSPΔ*H5*), with an N-terminal TEV (Tobacco Etch Virus) protease cleavable histidine tag, was a generous gift of the Zerbe lab (University of Zurich) given with permission from Gerhard Wagner (Harvard University). MSPΔH5 (pET-28a) was expressed in *E. coli* strain BL21(DE3) Star (Invitrogen, Carlsbad) using Terrific Broth medium. The culture was grown until $OD_{600}$ reached 0.8. Overexpression was induced by addition of 0.5 mM IPTG (Invitrogen, Carlsbad). After 30 min, the temperature was lowered to 28 °C for 4 h. The cells were harvested by centrifuging at 5000*g*, at 4 °C, for 10 min, and were resuspended in 100 mL of lysis buffer (20 mM Tris, pH 8, 5 mg Protein Inhibitor Tablets). After gentle stirring at 4 °C for 30 min, the cells were lysed by passing twice through the microfluidizer at a pressure of 42 psi. For the purification of MSPΔH5, previous protocols were followed.[49,50] Finally, MSPΔH5 was concentrated using an Amicon Ultra-4 10.000 Da molecular weight cutoff (MWCO) concentrator (Merck) to a concentration of 500 $\mu$M and was stored after freezing at −80 °C. $^{15}$N, $^2$H-labeled MSPΔH5 was expressed and purified as described before.[49]

**Preparation of DMPC14:1 Cholesterol Stock solution and Reconstitution of OmpX in MSPΔH5 Nanodiscs.** 9-*cis*-Unsaturated 1,2-dimyristoyl-*sn*-glycero-3-phosphocholine (termed DMPC14:1), its saturated counterpart (termed DMPC14:0), and cholesterol were purchased from Avanti Polar lipids. DMPC14:1 was mixed in a molar ratio of 4:1 and dissolved in chloroform (SigmaAldrich) in a glass vial. The solvent was removed under speed vacuum centrifugation at 3000 rpm, 37 °C, until a transparent homogeneous pellet was observed. The pellet was resuspended in a 200 mM sodium cholate (SigmaAldrich) solution until the solution was transparent. For the reconstitution of OmpX into MSPΔH5 nanodiscs, a molar ratio of 1:2:80:160 of OmpX/MSPdH5/lipids/sodium cholate was used. In the first step, the lipids, then the membrane protein, and finally MSPΔH5 was given in a glass vial and was gently shaken for 12 h at 27 °C. Then, 1 g of Biobeads SM-2 (Biorad) per mL of assembly solution was given to the mixture and was shaken for 5 h at 27 °C. Separation of the Biobeads was obtained by slow speed centrifugation. The supernatant was centrifuged for 2 min at 20 000*g* and then was purified over size exclusion chromatography as reported previously.[29] The fractions were concentrated using to a concentration of ∼300 $\mu$M using an Amicon Ultra-4 10.000 Da molecular weight cutoff (MWCO) concentrator (Merck).

**NMR Spectroscopy.** The experiments for OmpX were recorded at 316, 309, 303, 298, 293, 288, 283, and 278 K on a Bruker 600 MHz Avance III HD spectrometer with a cryogenic probehead. The number of scans was adjusted for each sample individually to achieve a satisfactory signal-to-noise ratio. All $^{15}$N protein relaxation experiments were recorded in an interleaved manner using 4 different relaxation delays, which were pseudorandomized (see Table 1 for delay times). A recovery delay of 7 s for the $R_1$ and 3 s for $R_2$ and $R2_{R1\rho}$ was used, with a spin-lock field of 2000 Hz during the $R2_{R1\rho}$ measurement.[33,34] The reported errors for $R_1$, $R_2$, and $R2_{R1\rho}$ are the standard deviation from the single exponential fit. For the chemical shift assignment of OmpX in DMPC14:1 nanodisc, a 3D TROSY-HNCA spectrum at 316 K using a standard Bruker pulse sequence (trhncaetgp2h3d) on a AV IIIHD 900 MHz spectrometer equipped with a cryoprobe was recorded. Since mostly only minor $^{13}$C chemical shift differences of OmpX in DMPC14:0 and DMPC14:1 were observed, a transfer of the $^{13}$C chemical shift assignment for most residues of OmpX in DMPC14:1 was possible. For the difference plot, relaxation rates at 293 and 309 K were scaled up using the $\tau_c$-ratios $\tau_{293\ K}/\tau_{316\ K}$ and $\tau_{309\ K}/\tau_{316\ K}$, respectively, to correct for the larger values due to slower tumbling at lower temperatures. The $\tau_c$-determined scaling factor was identical within 1% to a previously established scaling-method.[51] In contrast, $R_2$ and $R2_{R1\rho}$ values measured at 293 and 309 K were scaled down using the $\tau_c$-ratios $\tau_{316\ K}/\tau_{293\ K}$ and $\tau_{316\ K}/\tau_{309\ K}$ to compensate for the larger values due to slower tumbling at lower temperatures.

**Table 1. Delay Times for $^{15}$N Relaxation Measurements at Different Temperatures**

| expt | DMPC14:0 [ms] 316 K | DMPC14:1 [ms] 316 K | DMPC14:1 cholesterol [ms] 316 K |
|---|---|---|---|
| $R_1$ | 0, 1400, 1000, 400 | 0, 1400, 1000, 400 | 0, 1400, 1000, 400 |
| $R_{1\rho}$ | 1, 7.5, 15, 20 | 1, 20,10, 5 | 1, 20,10, 5 |
| $R_2$ | 0, 14, 7, 25 | 0, 45, 25, 10 | 0, 25, 15, 4 |
| | DMPC14:0 [ms] 309 K | DMPC14:1 [ms] 309 K | DMPC14:1 cholesterol [ms] 309 K |
| $R_1$ | 0, 1000, 600, 400 | 0, 1400, 1000, 400 | 0, 1200, 800, 400 |
| $R_{1\rho}$ | 1, 20,10, 5 | 1, 20,10, 5 | 1, 20,10, 5 |
| $R_2$ | 0, 21, 14, 7 | 0, 40, 20, 10 | 0, 40, 20, 10 |
| | | DMPC14:1 [ms] 293 K | |
| | $R_2$ | 0, 25, 15, 8 | |
| | $R_{1\rho}$ | 1, 15, 10, 5 | |

**$^{13}$C Natural Abundance Relaxation Experiments for Lipids.** $R_1$ inversion recovery and $R_2$ CPMG experiments for lipids were recorded at 316, 313, 309, 303, 298, 293, 288, 283, and 278 K on a Bruker 600 MHz Avance III HD spectrometer with a cryogenic probehead. For $R_1$ the 1D experiment "t1irpg" was used with 8 relaxation delays (0.01, 0.05, 0.5, 1, 2, 4, 8, and 10 s) and a recovery delay of 15 s. For $R_2$ the 1D experiment "cpmg" was modified to include $^1$H decoupling during the sequence. Eight relaxation delays were measured for each experiment using the delays 1, 5, 10, 15, 25, 50, 75, 100 ms for $\nu_{cpmg}$ = 2000 Hz; 4, 8, 16, 24, 32, 48, 72, and 104 ms for $\nu_{cpmg}$ = 125 Hz; and 2, 22, 42, 82, 122, 162, 202, and 242 ms for $\nu_{cpmg}$ = 250 Hz. The recovery delay was set to 5 s.



DOI: 10.1021/jacs.8b09188
J. Am. Chem. Soc. 2018, 140, 15402−15411

***Trans–Gauche* Isomerization.** For the calculation of the temperature influenced change of trans to gauche conformation of the lipid acyl chain lengths ($C_4$–$C_{11}$ atoms, Figure S5) a natural abundance $^{13}C$ spectrum was recorded on a AV IIIHD 600 MHz spectrometer using a standard Bruker pulse sequence (ineptrd) with a $^{1}H$ to $^{13}C$ magnetization transfer to avoid [$^{2}H$, $^{15}N$, $^{13}C$] OmpX contributions. The *trans–gauche* isomerization ($\Delta f_t$) was calculated by subtracting the chemical shifts of 29.5 ppm at 316 K from the one at 293 K and using the following relationships:[32,52]

$$\Delta\delta_{obs} = 5\ \text{ppm}(f_t - f_t')$$

$$\Delta f_t = \frac{\Delta\delta_{obs}}{5}$$

**Lipid Signal Intensity.** For the lipid signal intensity, temperature-dependent consecutive $^{1}H$ NMR (zggpw5) experiments were measured on AV IIIHD 600 MHz spectrometer. Then, the intensity at 1.45–1.25 ppm was distinguished and normalized by dividing with the intensity at 316 K. The decreasing signal intensities were fitted with a sigmoidal curve:

$$I = \frac{1}{1 + e^{(T_m - T)/R}}$$

with $T_m$ corresponding to the value at a residual signal intensity of 0.5 (representing the melting temperature), $I$ the lipid intensity ratio, $T$ the corresponding temperature, and $R$ a parameter defining the steepness of the curve, or in this case lipid cooperativity. The presence of lipid cooperativity justifies a sigmoidal curve fitting.[53,54] Fitting parameters were $T_m$ and $R$.

**Spectral Density Mapping.** Reduced spectral densities were calculated according to the following equations:[55]

$$J(0) = \frac{1}{3d^2 + 4c^2}[6R_2 - 3R_1 - 2.72\sigma_{NH}]$$

$$J(\omega_N) = \frac{1}{3d^2 + 4c^2}[4R_1 - 5\sigma_{NH}]$$

$$\sigma_{NH} = R_1(\text{NOE} - 1)\frac{\gamma_N}{\gamma_H}$$

$$d = \frac{1}{r^3}\frac{\mu_0 h\gamma_N\gamma_H}{8\pi^2}$$

$$c = \frac{\omega_N\Delta\sigma}{\sqrt{3}}$$

with $\mu_0$ as the permeability of vacuum, $\gamma_N$ and $\gamma_H$ as the gyromagnetic ratios of $^{15}N$ and $^{1}H$, $h$ as Planck constant, $\Delta\sigma$ as the chemical shift anisotropy, $\omega_N$ as the $^{15}N$ Larmor frequency, $r$ as the N–H distance, and NOE as the relative signal intensity of the $^{15}N[^{1}H]$ heteronuclear NOE (hetNOE) spectra measured in the presence and absence of $^{1}H$ saturation. Since the spectra of OmpX in all three lipid environments show a rigidly folded protein, we used the previously derived hetNOE-values from OmpX in DMPC14:0 also for OmpX in DMPC14:1 and DMPC14:1 with cholesterol for the rigidly folded $\beta$-strands.[29] With these values, $\sigma_{NH}$ was approximated for the reduced spectral density mapping. We acknowledge that the apparent dynamics changes in the different lipid environments at different temperatures also affect the hetNOE. However, hetNOE changes will influence $J(0)$ and $J(\omega_N)$ only marginally, since the hetNOE contributes only very little to $J(0)$ and $J(\omega_N)$. For example, a hetNOE change from 0.85 to 0.8 changes $\sigma_{NH}$ from 0.0045 to 0.006, which attributes 1.5% and 2% to the $R_1$ value (effectively influencing $\sigma_{NH}$ by less than 1%). Hence, $J(\omega_N)$ is largely (more than 98%) determined by $R_1$. Similarly, $R_1$ (e.g., with a value of 0.3 $s^{-1}$) is only about 0.5% of $R_2$ (e.g., with a value of 60 $s^{-1}$); hence, $J(0)$ is largely (more than 95%) determined by $R_2$, in agreement with previous estimations.[56]

For an isotropic tumbling with no internal motion, the spectral density function is given by

$$J(\omega) = \frac{2}{5}\left(\frac{\tau_c}{1 + (\omega\tau_c)^2}\right)$$

Hence, $J(0)$ is given by $2/5\tau_c$, with $\tau_c$ as the rotational correlation time.

Therefore, residues whose N–H bond dynamics are solely determined by a single motion, which is in this case the overall rotational motion of the molecule with its correlation time, will exhibit values that fall onto the curve:[51]

$$J(\omega_N) = \frac{J(0)}{1 + 6.25(\omega_N J(0))^2}$$

when plotting (correlating) $J(0)$ vs $J(\omega_N)$ values, using a value for $\omega_N$ of 0.377 rad/ns for a 14.1 T magnet. In contrast, residues with faster internal motions are shifted left to the curve exhibiting low $J(0)$ values, and residues with elevated microsecond to millisecond motions are shifted right to the curve exhibiting high $J(0)$ values.[51]

**Calculation Activation Energy.** By assuming that the temperature dependence of the rotational correlation time follows an Arrhenius relationship, the following formula can be used to calculate the activation energy $E_A$ of the rotational motion:[57]

$$\tau_c(T_1) = \tau_c(T_2)e^{[E_A/R(1/T_1 - 1/T_2)]}$$

with $R$ as the universal gas constant $T_1$ and $T_2$ as the two different temperatures.

**Determination of the Rotational Correlation Times $\tau_c$.** The rotational correlation time $\tau_c$ was measured on an AV IIIHD 600 MHz spectrometer at different temperatures using the [$^{15}N$, $^{1}H$]-TRACT pulse sequence,[58] where the slow relaxing $\alpha$-spin and fast relaxing $\beta$-spin state of $^{15}N$ were measured. From single exponential fits the bulk relaxation rates $R_\alpha$ and $R_\beta$ of the corresponding spin states were derived from an integral ($^{1}H$ ppm range 9.5–8.5 ppm), and the transverse cross-correlated relaxation rate $\eta_{xy}$ was determined as described previously and converted into the rotational correlation time $\tau_c$.[58]

## ■ ASSOCIATED CONTENT

### Supporting Information

The Supporting Information is available free of charge on the ACS Publications website at DOI: 10.1021/jacs.8b09188.

Additional figures including spectra densities, chemical shift information, and spectra (PDF)

## ■ AUTHOR INFORMATION


### Corresponding Authors

*roland.riek@phys.chem.ethz.ch

*stefan.bibow@unibas.ch

### ORCID

Sebastian Hiller: 0000-0002-6709-4684

Roland Riek: 0000-0002-6333-066X

Stefan Bibow: 0000-0003-1564-7045


### Notes

The authors declare no competing financial interest.

The peak assignment of OmpX in DMPC14:1 is deposited in the BMRB with the ID 27315.

## ■ ACKNOWLEDGMENTS

This work was supported by the Swiss National Science Foundation (grant numbers 167883, to S.B. and 163284 to R.R.) and the ETH Zurich.



DOI: 10.1021/jacs.8b09188
J. Am. Chem. Soc. 2018, 140, 15402–15411

## REFERENCES


(1) Alberts, B. *Molecular Biology of the Cell*; Garland Science: New York, 2002.
(2) Stryer, L. *Biochemistry*; W.H. Freeman: New York, 1995.
(3) van Meer, G.; Voelker, D. R.; Feigenson, G. W. *Nat. Rev. Mol. Cell Biol.* **2008**, *9*, 112.
(4) Lindahl, E.; Edholm, O. *J. Chem. Phys.* **2001**, *115*, 4938.
(5) Yeagle, P. L. *The Structure of Biological Membranes*; CRC Press, 2004.
(6) Marrink, S. J.; Risselada, J.; Mark, A. E. *Chem. Phys. Lipids* **2005**, *135*, 223.
(7) Nevzorov, A. A.; Brown, M. F. *J. Chem. Phys.* **1997**, *107*, 10288.
(8) Simons, K.; Sampaio, J. L. *Cold Spring Harbor Perspect. Biol.* **2011**, *3*, a004697.
(9) Yang, S. T.; Kreutzberger, A. J. B.; Lee, J.; Kiessling, V.; Tamm, L. K. *Chem. Phys. Lipids* **2016**, *199*, 136.
(10) Dufourc, E. *J. Chem. Biol.* **2008**, *1*, 63.
(11) Rog, T.; Pasenkiewicz-Gierula, M.; Vattulainen, I.; Karttunen, M. *Biophys. J.* **2007**, *92*, 3346.
(12) Weisz, K.; Grobner, G.; Mayer, C.; Stohrer, J.; Kothe, G. *Biochemistry* **1992**, *31*, 1100.
(13) Johannsson, A.; Smith, G. A.; Metcalfe, J. C. *Biochim. Biophys. Acta, Biomembr.* **1981**, *641*, 416.
(14) Dumas, F.; Tocanne, J. F.; Leblanc, G.; Lebrun, M. C. *Biochemistry* **2000**, *39*, 4846.
(15) Montecucco, C.; Smith, G. A.; Dabbeni-sala, F.; Johannsson, A.; Galante, Y. M.; Bisson, R. *FEBS Lett.* **1982**, *144*, 145.
(16) Martin, M.; de Mendoza, D. *Biochem. J.* **2013**, *451*, 269.
(17) Martens, C.; Stein, R. A.; Masureel, M.; Roth, A.; Mishra, S.; Dawaliby, R.; Konijnenberg, A.; Sobott, F.; Govaerts, C.; McHaourab, H. S. *Nat. Struct. Mol. Biol.* **2016**, *23*, 744.
(18) Gao, Y.; Cao, E.; Julius, D.; Cheng, Y. *Nature* **2016**, *534*, 347.
(19) Baenziger, J. E.; Darsaut, T. E.; Morris, M. L. *Biochemistry* **1999**, *38*, 4905.
(20) Gracheva, E. O.; Cordero-Morales, J. F.; Gonzalez-Carcacia, J. A.; Ingolia, N. T.; Manno, C.; Aranguren, C. I.; Weissman, J. S.; Julius, D. *Nature* **2011**, *476*, 88.
(21) Gracheva, E. O.; Ingolia, N. T.; Kelly, Y. M.; Cordero-Morales, J. F.; Hollopeter, G.; Chesler, A. T.; Sanchez, E. E.; Perez, J. C.; Weissman, J. S.; Julius, D. *Nature* **2010**, *464*, 1006.
(22) Frauenfelder, H.; Chen, G.; Berendzen, J.; Fenimore, P. W.; Jansson, H.; McMahon, B. H.; Stroe, I. R.; Swenson, J.; Young, R. D. *Proc. Natl. Acad. Sci. U. S. A.* **2009**, *106*, 5129.
(23) Lewandowski, J. R.; Halse, M. E.; Blackledge, M.; Emsley, L. *Science* **2015**, *348*, 578.
(24) Hagn, F.; Etzkorn, M.; Raschle, T.; Wagner, G. *J. Am. Chem. Soc.* **2013**, *135*, 1919.
(25) Frauenfeld, J.; Gumbart, J.; Sluis, E. O.; Funes, S.; Gartmann, M.; Beatrix, B.; Mielke, T.; Berninghausen, O.; Becker, T.; Schulten, K.; Beckmann, R. *Nat. Struct. Mol. Biol.* **2011**, *18*, 614.
(26) Bibow, S.; Carneiro, M. G.; Sabo, T. M.; Schwiegk, C.; Becker, S.; Riek, R.; Lee, D. *Protein Sci.* **2014**, *23*, 851.
(27) Lakomek, N. A.; Frey, L.; Bibow, S.; Bockmann, A.; Riek, R.; Meier, B. H. *J. Phys. Chem. B* **2017**, *121*, 7671.
(28) Kofuku, Y.; Ueda, T.; Okude, J.; Shiraishi, Y.; Kondo, K.; Mizumura, T.; Suzuki, S.; Shimada, I. *Angew. Chem., Int. Ed.* **2014**, *53*, 13376.
(29) Frey, L.; Lakomek, N. A.; Riek, R.; Bibow, S. *Angew. Chem., Int. Ed.* **2017**, *56*, 380.
(30) Martinez, D.; Decossas, M.; Kowal, J.; Frey, L.; Stahlberg, H.; Dufourc, E. J.; Riek, R.; Habenstein, B.; Bibow, S.; Loquet, A. *ChemPhysChem* **2017**, *18*, 2651.
(31) Mors, K.; Roos, C.; Scholz, F.; Wachtveitl, J.; Dotsch, V.; Bernhard, F.; Glaubitz, C. *Biochim. Biophys. Acta, Biomembr.* **2013**, *1828*, 1222.
(32) Brainard, J. R.; Knapp, R. D.; Morrisett, J. D.; Pownall, H. J. *J. Biol. Chem.* **1984**, *259*, 10340.
(33) Lakomek, N. A.; Kaufman, J. D.; Stahl, S. J.; Louis, J. M.; Grishaev, A.; Wingfield, P. T.; Bax, A. *Angew. Chem., Int. Ed.* **2013**, *52*, 3911.
(34) Lakomek, N. A.; Ying, J.; Bax, A. *J. Biomol. NMR* **2012**, *53*, 209.
(35) Ahyayauch, H.; Larijani, B.; Alonso, A.; Goni, F. M. *Biochim. Biophys. Acta, Biomembr.* **2006**, *1758*, 190.
(36) Liang, B.; Arora, A.; Tamm, L. K. *Biochim. Biophys. Acta, Biomembr.* **2010**, *1798*, 68.
(37) Lenaz, G. *Biosci. Rep.* **1987**, *7*, 823.
(38) Klauda, J. B.; Roberts, M. F.; Redfield, A. G.; Brooks, B. R.; Pastor, R. W. *Biophys. J.* **2008**, *94*, 3074.
(39) Leftin, A.; Brown, M. F. *Biochim. Biophys. Acta, Biomembr.* **2011**, *1808*, 818.
(40) Pastor, R. W.; Venable, R. M.; Karplus, M.; Szabo, A. *J. Chem. Phys.* **1988**, *89*, 1128.
(41) Shaw, A. W.; McLean, M. A.; Sligar, S. G. *FEBS Lett.* **2004**, *556*, 260.
(42) Abyzov, A.; Salvi, N.; Schneider, R.; Maurin, D.; Ruigrok, R. W.; Jensen, M. R.; Blackledge, M. *J. Am. Chem. Soc.* **2016**, *138*, 6240.
(43) Rog, T.; Pasenkiewicz-Gierula, M.; Vattulainen, I.; Karttunen, M. *Biochim. Biophys. Acta, Biomembr.* **2009**, *1788*, 97.
(44) Meier, P.; Sachse, J. H.; Brophy, P. J.; Marsh, D.; Kothe, G. *Proc. Natl. Acad. Sci. U. S. A.* **1987**, *84*, 3704.
(45) Michonova-Alexova, E. I.; Sugar, I. P. *Biophys. J.* **2002**, *83*, 1820.
(46) Smith, R. L.; Oldfield, E. *Science* **1984**, *225*, 280.
(47) Fersht, A. *Structure and Mechanism in Protein Science: A Guide to Enzyme Catalysis and Protein Folding*; World Scientific, 1999.
(48) Fernandez, C.; Adeishvili, K.; Wuthrich, K. *Proc. Natl. Acad. Sci. U. S. A.* **2001**, *98*, 2358.
(49) Bibow, S.; Polyhach, Y.; Eichmann, C.; Chi, C. N.; Kowal, J.; Albiez, S.; McLeod, R. A.; Stahlberg, H.; Jeschke, G.; Guntert, P.; Riek, R. *Nat. Struct. Mol. Biol.* **2017**, *24*, 187.
(50) Tzitzilonis, C.; Eichmann, C.; Maslennikov, I.; Choe, S.; Riek, R. *PLoS One* **2013**, *8*, e54378.
(51) Krizova, H.; Zidek, L.; Stone, M. J.; Novotny, M. V.; Sklenar, V. *J. Biomol. NMR* **2004**, *28*, 369.
(52) Purusottam, R. N.; Senicourt, L.; Lacapere, J. J.; Tekely, P. *Biochim. Biophys. Acta, Biomembr.* **2015**, *1848*, 3134.
(53) Faiss, S.; Schuy, S.; Weiskopf, D.; Steinem, C.; Janshoff, A. *J. Phys. Chem. B* **2007**, *111*, 13979.
(54) Nagarajan, S.; Schuler, E. E.; Ma, K.; Kindt, J. T.; Dyer, R. B. *J. Phys. Chem. B* **2012**, *116*, 13749.
(55) Bracken, C.; Carr, P. A.; Cavanagh, J.; Palmer, A. G., 3rd *J. Mol. Biol.* **1999**, *285*, 2133.
(56) Kneller, J. M.; Lu, M.; Bracken, C. *J. Am. Chem. Soc.* **2002**, *124*, 1852.
(57) Good, D.; Pham, C.; Jagas, J.; Lewandowski, J. R.; Ladizhansky, V. *J. Am. Chem. Soc.* **2017**, *139*, 9246.
(58) Lee, D.; Hilty, C.; Wider, G.; Wuthrich, K. *J. Magn. Reson.* **2006**, *178*, 72.



DOI: 10.1021/jacs.8b09188
*J. Am. Chem. Soc.* 2018, 140, 15402−15411